Editors' Suggestion

Altermagnetic nanotextures revealed in bulk MnTe

Rikako Yamamoto,[1,2,*] Luke Alexander Turnbull,[1,2] Marcus Schmidt,[1] José Claudio Corsaletti Filho,[1] Hayden Jeffrey Binger,[1] Marisel Di Pietro Martínez,[1,2] Markus Weigand,[3] Simone Finizio,[3,4] Yurii Prots,[1] George Matthew Ferguson,[1] Uri Vool,[1] Sebastian Wintz,[3] and Claire Donnelly[1,2,†]

[1] *Max Planck Institute for Chemical Physics of Solids, 01187 Dresden, Germany*
[2] *International Institute for Sustainability with Knotted Chiral Meta Matter (WPI-SKCM²), Hiroshima University, Hiroshima 739-0046, Japan*
[3] *Institute for Nanospectroscopy, Helmholtz-Zentrum Berlin, 12489 Berlin, Germany*
[4] *Swiss Light Source, Paul Scherrer Institute, 5232 Villigen PSI, Switzerland*

(Received 26 February 2025; revised 4 July 2025; accepted 29 July 2025; published 16 September 2025)

Altermagnetism represents a magnetic phase in which the combination of compensated antiferromagnetic order with an anisotropic crystal field leads to time-reversal symmetry breaking. The resulting combination of properties typically associated with ferromagnets, but with net-zero magnetization, has generated significant interest for both fundamental research and technological applications. With many candidate altermagnetic materials, MnTe has emerged as one of the most promising systems, with growing experimental evidence for altermagnetic phenomena. So far, the majority of measurements have been performed on thin films, or have involved surface measurements. However, the question of altermagnetic order in the bulk system—in the absence of substrate or surface effects—remains. Here we show evidence for bulk altermagnetism in single-crystal MnTe through spectroscopic x-ray microscopy. By performing nanoscale x-ray magnetic circular dichroic (XMCD) imaging in transmission on a 200-nm-thick lamella, we observe domains and magnetic textures with a spectroscopic signature characteristic of altermagnetic order, thereby confirming the intrinsic nature of altermagnetism in MnTe. Quantitative analysis of the XMCD signal reveals excellent agreement with predicted signals, establishing that the altermagnetic order exists throughout the thickness of the lamella and confirming the intrinsic, bulk nature of the state. With these results, we demonstrate that transmission XMCD spectroscopic imaging is a robust, quantitative technique to probe altermagnetic order, providing a means to probe individual altermagnetic domains within complex configurations. This ability to investigate and characterize altermagnetic order in bulk crystals represents an important tool for the exploration of altermagnetism across a wide range of candidate materials, of key importance for the development of future technologies.

DOI: 10.1103/dp7v-qszq

I. INTRODUCTION

Magnetism has played an important role in society, from ferromagnets that have led to the generation of electricity and more recently facilitated the information age, to the more recently discovered antiferromagnets that offer a route to robust terahertz technologies. When it comes to spintronic applications, identifying the optimal type of magnetic order is important [1]. On the one hand, ferromagnets exhibit strong spintronic effects such as the anomalous Hall effect (AHE) and giant magnetoresistance, allowing their magnetic configuration to be efficiently read and written [2]. However, their net magnetization makes them susceptible to external magnetic fields, and their dynamic response, which determines information transfer speeds, is limited to the gigahertz range [3]. On the other hand, antiferromagnets have zero net magnetization, making them highly robust and enabling technologically relevant terahertz dynamics [4,5]. However, despite first demonstrations of all-electrical reading and writing of antiferromagnetic order [6], their spintronic signals are generally weak, limiting their potential applications.

Altermagnets provide a possible solution to this problem [7,8], as they combine features of ferro- and

*Contact author: rikako.yamamoto@cpfs.mpg.de
†Contact author: claire.donnelly@cpfs.mpg.de

antiferromagnets (see Fig. 1) that are of importance for potential spintronic applications. In particular, an altermagnet has a collinear compensated spin configuration, which is associated, as in broader antiferromagnets, with net zero magnetization, and ultrafast dynamics on the subpicosecond timescale [9]. However, compared to antiferromagnets, there is an additional symmetry breaking associated with the local environment of each sublattice, as shown in Fig. 1(c). This gives rise to unconventional spin splitting of the bands in momentum space, which in turn can result in measurable spintronic signals such as AHE and tunneling magnetoresistance effects (albeit for certain orientations of the Néel vector). These materials thus promise to combine the robust, ultrafast nature of antiferromagnets with ferromagneticlike phenomena, representing an opportunity for future technological applications [10].

This concept of altermagnetism as a third form of ferroic magnetic order was first defined by considering the spin and crystal symmetries separately [7], which allowed for a complete classification of all the possible spin arrangements on crystals, and the identification of altermagnetic phases with *d*-, *g*-, and *i*-wave spin order in momentum space. This discovery was motivated by previous observations of anomalies such as Hall effects in collinear antiferromagnetic order [11–14], spin-current generation [15,16] and unconventional spin splittings [17–23]. We note that both AHE [24–26] and circular dichroism [27,28] were previously reported in noncollinear compensated magnets. However, the remarkable fact of altermagnets is that they are able to exhibit such phenomena even with a simple collinear compensated spin structure.

Since the first prediction of altermagnetism [7], these symmetry arguments have been used to predict a wide variety of known—and unknown—materials to be altermagnetic. This has led to renewed interest in materials that in some cases have long been studied, specifically now looking for evidence of altermagnetism. Indeed, first experimental indications of altermagnetism were given by the presence of an AHE in a variety of collinear compensated magnets [11,14,29–31], in which such an effect would not traditionally be expected [32]. Direct evidence of time-reversal symmetry breaking was provided by the band splitting in momentum space measured by angle-resolved photoemission spectroscopy [33]. Subsequent x-ray magnetic circular dichroic (XMCD) measurements in altermagnets [34], again an effect that would not traditionally be expected for antiferromagnetic materials, allowed for the direct imaging of altermagnetic nanoscale order—both domains, domain walls, and topological textures [35]. Indeed, the XMCD itself provides evidence of time-reversal symmetry breaking, not only providing access to nanoscale configurations, but also allowing one to probe the altermagnetic nature of the material.

With the growing number of theoretical and experimental works, the next challenge lies in identifying and confirming candidate altermagnetic materials. Initially, studies focused on the candidate RuO_2, one of several proposed candidates [36], a collinear antiferromagnet with the rutile structure. Despite first measurements in thin films that suggested antiferromagnetic ordering [37,38], the presence of AHE [14] and spin splitting [39,40] characteristic of altermagnets, it has remained challenging to conclusively determine the nature of the material in the bulk [41–43]. Recently, MnTe has emerged as the next promising candidate. It has long been known to be a collinear antiferromagnet, as established by neutron diffraction [44], and through symmetry arguments was suggested as a candidate material for altermagnetism [7]. First measurements on thin-film systems grown by molecular beam epitaxy (MBE) [9,33,35,45] revealed the successful measurement of spin splitting in momentum space [33,45], as well as the existence of circular dichroism [34,35]. While the vast majority of transport measurements of the AHE have been mainly focused on thin-film systems [29], recent measurements of bulk MnTe have also reported the AHE, albeit with certain discrepancies with respect to thin-film systems [31], and circular dichroism has also been measured on single crystals with resonant inelastic x-ray scattering [46]. As well as these discrepancies between the bulk and the thin-film measurements, indications of the influence of substrate-induced strain have been observed both in transport measurements [47], as well as in nanoscale XMCD imaging, where lithographic patterning appears to result in local strain relaxation for the manipulation of the order [35]. In this context, disentangling the role of the substrate or surface in thin films or surface-sensitive measurements, and the resulting local strain and symmetry breaking, is highly important to clarifying the intrinsic altermagnetic nature of MnTe [48–50].

Here we obtain experimental evidence of bulk altermagnetism in a lamella extracted from a single crystal of MnTe with nanoscale x-ray spectroscopic imaging. We observe magnetic domains and textures with XMCD that exhibit the characteristic three-fold symmetry expected for MnTe. We measure an associated spectroscopic XMCD signal that changes sign multiple times across the Mn $L_{2,3}$ edges. This oscillating signal is characteristic of altermagnetic MnTe, and exhibits remarkable quantitative agreement with theoretical calculations [34]. By measuring a free-standing lamella in transmission, we integrate through the material, providing evidence that altermagnetic order exists in the absence of surface effects and substrate-induced strain. This, combined with the quantitative agreement of the measured dichroism with theoretical calculations, indicates that the altermagnetic order exists within the bulk of the material, thus providing evidence for the intrinsic nature of altermagnetism in MnTe. Such transmission XMCD measurements represent an important tool to understand altermagnetic order in bulk samples and open up the *in situ* study of altermagnets under the application

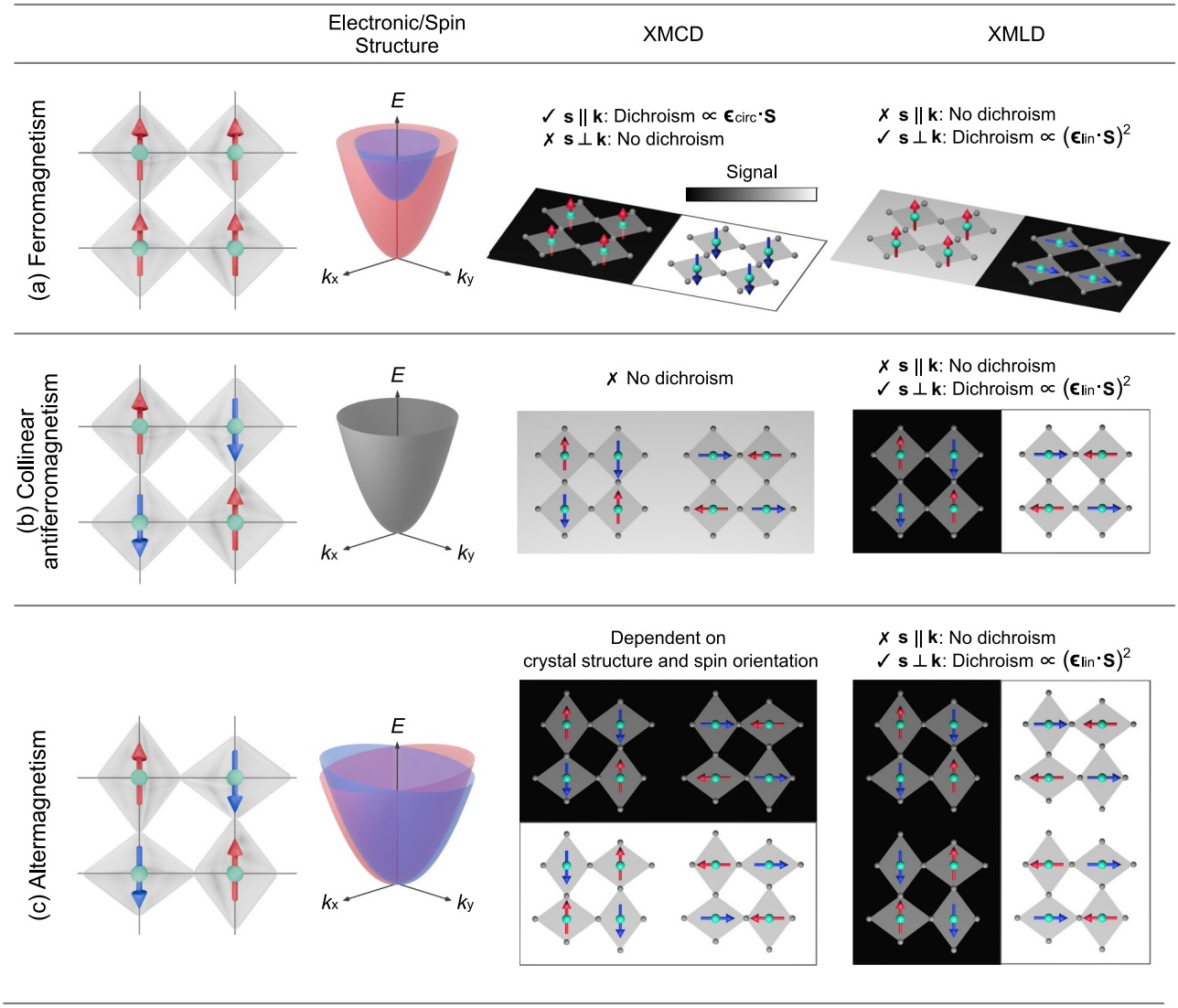

FIG. 1. Mapping magnetic domains in ferromagnets, antiferromagnets, and altermagnets using polarized x-rays. The spin configuration and local crystal environments of ordered magnetic ions (left), the electronic and spin structure in momentum space (center), and the expected x-ray magnetic circular dichroic (XMCD) and x-ray magnetic linear dichroic (XMLD) contrast for different domain configurations (right) are shown for (a) ferromagnetism, (b) antiferromagnetism, and (c) *d*-wave altermagnetism. Throughout, red and blue indicate opposite spin orientations, while the black, and white, and gray planes in the XMCD/XMLD schematics indicate positive, negative, and zero XMCD or XMLD intensity, respectively. We note that these spin orientations are shown schematically to provide an overview of the phenomena, and that the particular symmetry dependence of the XMCD for altermagnets should be considered in detail for each material. (a) In ferromagnets, neighboring spins have parallel alignment, associated with a well-defined splitting in momentum space. For spins orientated collinear to the direction of the x-rays (**s** ∥ **k**), there is a nonzero XMCD with respect to the x-ray linear polarization $\boldsymbol{\epsilon}_{\mathrm{circ}}$. XMLD can be used to distinguish spins with perpendicular orientation, depending on the orientation of the spin with respect to the x-ray linear polarization $\boldsymbol{\epsilon}_{\mathrm{lin}}$. (b) For collinear antiferromagnets with in-plane spin configuration (**s** ⊥ **k**), neighboring spins have antiparallel alignment, with no associated spin splitting in momentum space. There is no XMCD signal associated with this state, however XMLD distinguishes between perpendicular spin configurations in the plane perpendicular to the x-ray direction. (c) In altermagnets, magnetic domains form due to the combination of antiferromagnetic spin configurations, and inequivalent local environments. Here we show the example of a *d*-wave altermagnet for simplicity, where four types of magnetic domains can be identified. The XMCD signal depends on the spin orientation with respect to the local crystal environment, as well as the spin orientation with respect to the x-ray direction and, if present, distinguishes between different domain orientations. We note that this symmetry and x-ray orientation dependence is different for *d*-wave and *g*-wave altermagnets such as MnTe, for which there are six different types of magnetic domains with respect to the easy axes [see Figs. 2(c) and 2(d)]. Altermagnets also exhibit linear dichroism, which probes the relative orientation of the spins with respect to the linear polarization of the light.

of external stimuli such as magnetic fields and currents, for both the probing of fundamental characteristics and the development of future technologies.

II. XMCD IN ALTERMAGNETS

To probe the altermagnetic nature of MnTe in the bulk, we turn to x-ray magnetic circular dichroism. An overview of magnetic dichroism for different types of magnetic order—ferromagnetic, antiferromagnetic and altermagnetic—is given in Fig. 1. Commonly associated with ferromagnets, XMCD represents the difference in the scattering factor and absorption cross section of x-rays for circular left- and right-handed light, in the vicinity of an absorption edge. For collinear antiferromagnets, which have zero net magnetization, there is typically no circular dichroism. Instead, linear magnetic dichroism, where the scattering factor depends on the relative orientation of the polarization of the light and the Néel vector, can be used to probe the local order, as shown in Fig. 1(b). Remarkably, altermagnets exhibit not only the expected linear dichroism due to the orientation of the Néel vector, but also XMCD [see Fig. 1(c)]. This circular dichroism is not due to a net magnetic moment in the system, but is of different origin from the ferromagnetic case.

The origin of XMCD for altermagnetic materials is generally associated with time-reversal symmetry breaking, and has been understood in the context of the Hall vector which the XMCD effectively probes [34,35]. One must note that the existence of XMCD is not a defining property of altermagnets: indeed, the presence of XMCD depends strongly on the orientation of the collinear antiferromagnetically aligned spins, meaning that XMCD will typically only be present for certain orientations of the Néel vector.

For the case of MnTe it has been shown that these different origins of circular dichroism—that associated with the net magnetization, and the dichroism associated with the altermagnetic order—can be distinguished by their spectroscopic nature [34]. As a result, spectroscopic measurements of XMCD offer a route to probing the altermagnetic order of materials.

III. MEASURING XMCD IN BULK MANGANESE TELLURIDE

To probe the bulk altermagnetism in MnTe, we fabricate a lamella of thickness ranging from 150 to 200 nm extracted from bulk single-crystal MnTe with focused ion beam. The crystal [shown in Fig. 2(a)] was grown with chemical vapor transport [51], and the lamella was extracted such that it is oriented perpendicular to the *c* axis, with the *a* and *b* axes lying in the plane. The relative orientation of the *a* and *b* axes with respect to the lamella is indicated in Figs. 3(b) and 3(c). More details of the crystal growth, characterization, and lamella preparation are given in the Appendix. The three-dimensional crystal structure

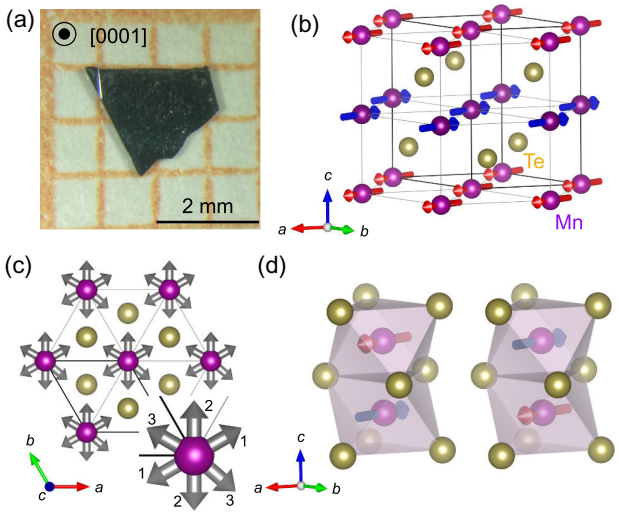

FIG. 2. Crystal structure and magnetic order of MnTe. (a) Bulk MnTe crystal grown with chemical vapor transport. (b) Crystallographic and magnetic structure of MnTe (c) Three easy antiferromagnetic spin axes of MnTe. (d) Taking the three-dimensional crystal structure surrounding the Mn atoms into account, one can distinguish altermagnetic domains with opposite sublattice orientation that are related by time-reversal symmetry.

around the Mn atoms, and the different sublattices, are shown in Fig. 2. Due to the hexagonal crystal structure and anisotropy, the antiferromagnetic moments lie in the *ab*-plane, as shown in Figs. 2(b) and 2(c), with three easy axes along which the Néel vector in the antiferromagnetic domains typically orients [52,53]. The two collinear antiferromagnetic sublattices of MnTe are related by mirror symmetry, rather than a simple translation or inversion. As a result, the two domains are related by time-reversal symmetry, satisfying the symmetry classification of altermagnetism. For altermagnets, XMCD can exist for certain orientations of the Néel vector. In MnTe, these orientations correspond to the spins aligning along the $[1\bar{1}10]$ orientations [34], providing an orientation-dependent XMCD signal for the spins in the *ab*-plane.

Quantitative measurements of the XMCD signal through the thickness of the lamella were obtained with scanning transmission x-ray microscopy (STXM) at the MAXYMUS beamline at BESSY II. The STXM setup is shown schematically in Fig. 3(a). X-ray optics are used to focus the x-ray probe to a spot size of 25 nm. The sample is then scanned with respect to the beam, and the transmitted photons recorded at each point. By performing scans with circular left- and right-polarized light in the vicinity of the Mn $L_{2,3}$ edges, one can obtain a projection of the XMCD signal with nanoscale resolution, that integrates through the thickness of the lamella parallel to the *c* axis of MnTe. Measurements were performed at a temperature of 100 K, sufficiently below the Néel temperature of 307 K,

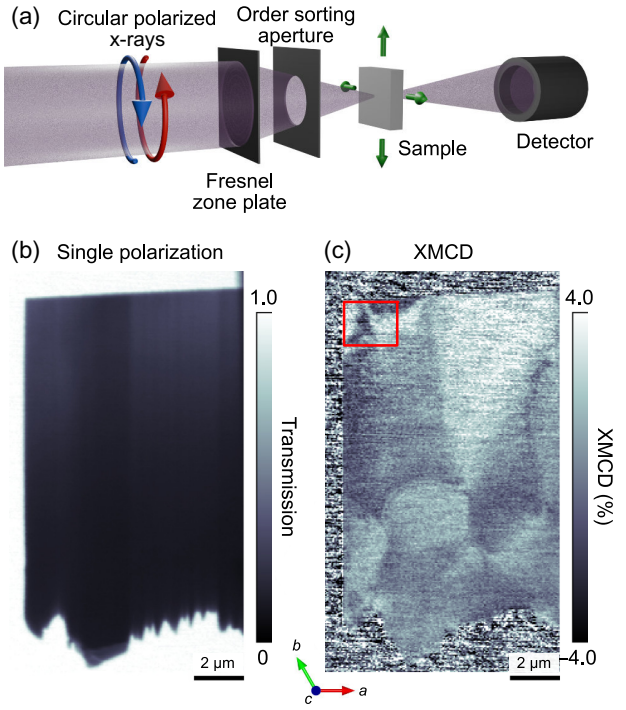

FIG. 3. X-ray magnetic circular dichroic scanning transmission x-ray microscopy (STXM) of altermagnetic domains in MnTe. (a) Schematic of STXM setup, where circularly polarized x-rays are focused onto a sample that is scanned to acquire a transmission projection with nanoscale resolution. (b) A single polarization projection of the lamella, and (c) an XMCD projection of the lamella, showing different regions with dark and bright contrast indicating the presence of domains and magnetic features.

where both XMCD and AHE signals have previously been measured [29,34,35].

The presence of XMCD in the lamella was confirmed by performing XMCD STXM with an x-ray energy of 640.30 eV, 0.75 eV below the energy corresponding to maximum absorption at the Mn L_3 absorption edge. The electronic and XMCD images of the MnTe lamella are given in Figs. 3(b) and 3(c), respectively (see Appendix for details of XMCD calculation). In the XMCD image, one can immediately see bright and dark XMCD contrast varying throughout the lamella.

IV. XMCD SPECTROSCOPIC ANALYSIS

To determine whether our observed XMCD signal is associated with altermagnetic order, we perform XMCD spectromicroscopy across the Mn-$L_{2,3}$ edges, following the energy evolution of the XMCD contrast of the domain features. A series of XMCD projections of a zoomed region of the lamella taken across the L_3 and L_2 edges is shown in Figs. 4(a) and 4(b), respectively. As one traverses both edges, one can see the domain features changing contrast a total of eight times across the L_3 edge, and twice across the L_2 edge, consistent with the oscillating contrast of altermagnetic order in MnTe [34]. An XMCD spectrum, measured in a single domain region with an energy step size of 0.05 eV in the vicinity of the $L_{2,3}$ edges, is plotted with a dashed line in Fig. 4(c) alongside the absorption spectrum (solid line), and confirms this oscillating signal. We can extract XMCD signals from the set of images measured across the edge by comparing the signal within domains of opposite contrast. This XMCD contrast is calculated quantitatively as a percentage of the maximum absorption of the material at the L_3 edge, defined as $A_{\max}$ in Fig. 4(c), and is plotted alongside the spectrum in Fig. 4(c). Not only does the XMCD contrast qualitatively agree with spectra calculated using a local density approximation and dynamical mean-field theory (LDA+DMFT) and Anderson impurity model (AIM) approach [54–56], with the XMCD contrast exhibiting nine peaks of alternating sign across the L_3 edge [34]; a remarkable agreement is observed in the quantitative signal as well. Indeed, previous spectroscopic measurements reported an order-of-magnitude difference between the magnitude of the predicted and measured altermagnetic XMCD signal [34]. Here, we observe a maximum XMCD contrast of $1.8 \pm 0.3\%$ of $A_{\max}$, the maximum absorption, which agrees well with the predicted XMCD contrast of 1.8% of $A_{\max}$ [34].

This quantitative agreement between the theoretical calculations of XMCD and the spectra measured here allows us to draw two main conclusions. First, by measuring the spectrum with nanoscale spatial resolution, we remove the effect of averaging over domains, and instead can extract a signal that can be quantitatively compared with theory. Second, the quantitative agreement between our data and the calculations by the LDA+DMFT AIM calculations, when compared to the absorption of the material, allows us to determine whether the XMCD signal originates from ordering at the surface of the sample or exists through the bulk of the lamella. Indeed, if we consider the two cases of a surface altermagnetic order and a bulk altermagnetic order, shown schematically in Fig. 4(d), a large discrepancy in the measured value of the XMCD would be expected. For a surface effect, where we assume the surface order to be limited to around 10 nm of the surface, the XMCD signal would be expected to account for less than 0.2% of the total absorption of the sample. For the bulk order, and a continuous domain through the sample, the XMCD signal should correspond to approximately 1–2% of the total absorption, as we observe here. As a result, we can conclude that in our crystalline MnTe sample, the altermagnetic order exists in the bulk of the lamella of 200 nm thickness.

V. ALTERMAGNETIC CONFIGURATION

Having confirmed that the bulk MnTe exhibits altermagnetic order, we next consider the domain configuration

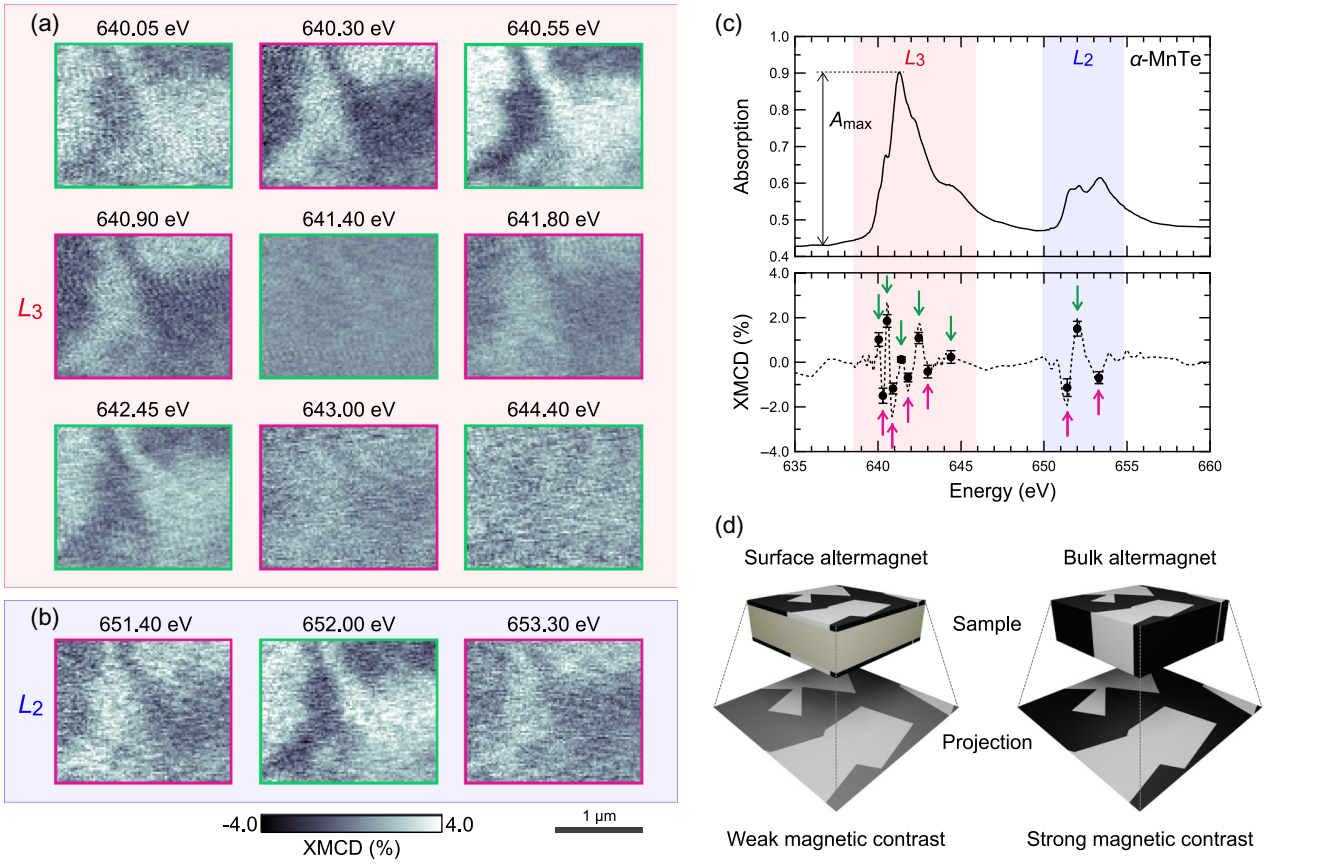

FIG. 4. XMCD spectromicroscopy across the Mn $L_{2,3}$ edges. (a) A zoomed region of the lamella [corresponding to the box in Fig. 3(c)] is shown for nine energies across the L_3 edge, across which the contrast can be seen to switch eight times. Note that lower contrast is observed for energies on the absorption edge (641.4 eV and 641.8 eV) that is likely due to high absorption of the sample. (b) The same region is shown for three energies across the L_2 edge, where the contrast can be seen to switch twice. (c) The x-ray absorption spectrum (solid line) and the XMCD spectrum (dashed line) acquired on a single domain within the lamella are plotted, along with the XMCD contrast extracted from the images shown in (a) and (b) (black dots, highlighted by green and purple arrows). (d) Schematic of the expected contrast of (left) surface and (right) bulk altermagnetic order in transmission. The quantitative agreement of the XMCD signal with LDA+DMFT AIM calculations presented in Ref. [34] indicates the bulklike nature of the altermagnetic order.

present in the lamella. As observed in Fig. 3(c), a number of regions with bright and dark XMCD can be observed. In MnTe, the XMCD is closely linked to the symmetry of the magnetic order. In particular, the XMCD is expected to vary as a function of the orientation of the Néel vector in the *ab*-plane and exhibit three-fold rotational symmetry [35], as shown schematically in the inset of Fig. 5(b). As a result, a change in XMCD contrast indicates a rotation of the Néel vector and the formation of altermagnetic domains.

A. Altermagnetic domains

We first consider the overall configuration of the lamella, which appears to host a rather complex domain structure. Notably, the domain size is generally of the order of micrometres in size. This is significantly larger than the domains observed in thin films grown by MBE [35], and could be due to the difference in microstructure or strain between the single-crystal lamella measured here and the thin films. Indeed, in our lamella, we notice that the domain size varies between the center of the lamella—where the domains are relatively large, of the order of 5 μm—and the edges, where smaller domains of the order of 1 μm form. To understand this variation in the size of the domains, we can consider two main differences between the edge and the center. First, surface effects such as slight differences in the strain distribution are present, which have been shown to influence antiferromagnetic [57,58] and altermagnetic configurations [35]. Secondly, due to the fabrication process, the edges of the lamella are more likely to contain defects. As in an antiferromagnet, strain, disorder, or structural defects often lead to the formation of domains that otherwise would not be energetically favorable [59]. We therefore conclude that both edge-strain effects and microstructural defects could play a role in determining the size of the altermagnetic domains.

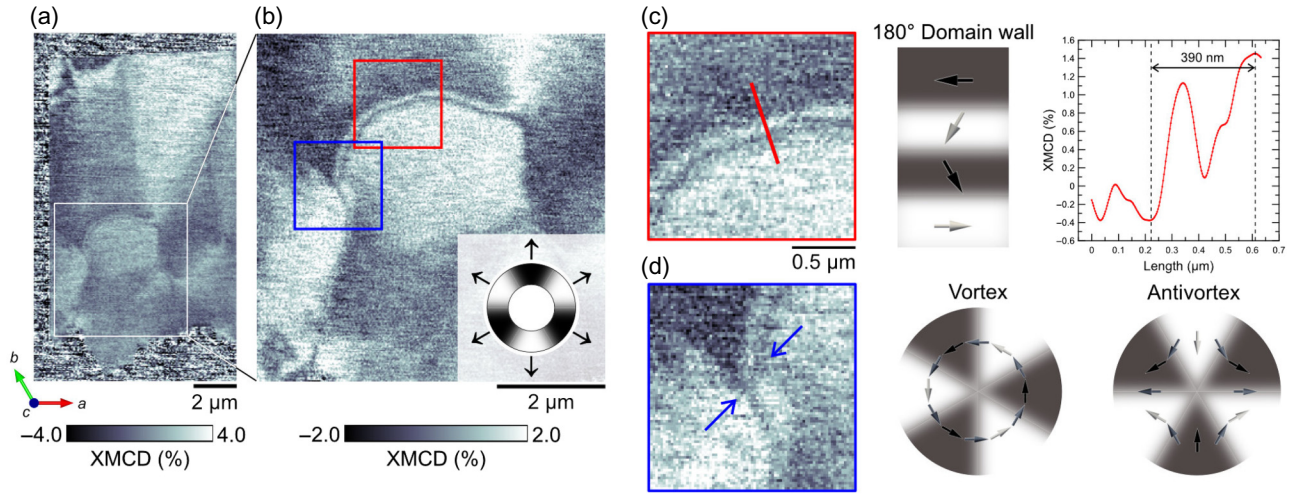

FIG. 5. Altermagnetic domain configurations and nanotextures. (a) Overview of the domain configuration within the lamella. (b) A zoom of the region indicated by the white box in (a) reveals a number of nanoscale features within the configuration, where the XMCD changes rapidly. The XMCD contrast depends on the in-plane orientation of the Néel vector with three-fold symmetry, as indicated by the contrast wheel in the inset. (c) A closer look at the configuration highlighted by the red box in (b) reveals an elongated structure indicated by the red line, across which the XMCD contrast reverses from white to black to white to black. Considering the angular dependence of the XMCD, this contrast is consistent with the presence of a 180° Néel domain wall, as shown schematically. This oscillating contrast can be seen in a line profile of the XMCD taken across the domain wall, revealing the domain wall width to be 390 nm. (d) Considering the configuration highlighted by the blue box in (b), one can see two features in the XMCD (indicated by blue arrows) that resemble a cartwheel-like contrast, with three-fold rotational symmetry. Such contrast is consistent with the presence of a winding texture, which could be a vortex or an antivortex, as shown schematically. However, with the XMCD signal alone, it is not possible to determine exactly which configuration is present.

In addition to the change in the size of the domains, we note that the XMCD is not a homogeneous bright or dark contrast throughout the sample—which would be associated with the Néel vector aligning along the three easy axes in the *ab*-plane. The presence of the intermediate gray contrast could be consistent with the orientation of the Néel vector pointing away from a principal axis [34], consistent with a low anisotropy in the plane, and the smooth variation of the magnetic moment orientations. Alternatively, as we are integrating through the sample, the contrast could arise from an unresolved three-dimensional domain structure [60].

B. Altermagnetic textures

As well as the presence of magnetic domains that can be identified as regions of homogeneous XMCD contrast, there exist a number of features in the XMCD projection that indicate the presence of nanoscale textures of the Néel vector. In the first work harnessing XMCD-photoelectron emission microscopy to image the magnetic configuration of an altermagnet, vortices, antivortices, and domain walls of the Néel vector could be identified by their XMCD and x-ray magnetic linear dichroism contrast in thin-film MnTe, and indeed could even be controlled by the micropatterning of the thin film [35]. Here, we consider a number of features in the region of the lamella indicated by the white box in Fig. 5(a), and shown in more detail in Figs. 5(b)–5(d). Specifically, we consider two features in more detail. The first of these is an elongated wall that appears between black and white domains, highlighted by the red box in Fig. 5(b) and shown in (c). Across the boundary between the two domains, the XMCD contrast does not switch simply from black to white, but rather alternates black–white–black–white across a distance of 390 nm. When considering the dependence of the XMCD contrast on the direction of the Néel vector in the schematic, one can see that such contrast is consistent with a 180° domain wall of the Néel vector with a width of 390 nm, across which the XMCD contrast switches due to the reversal of the sublattice moments. Multiple such 180° domain walls were observed in this configuration, as well as other configurations within additional lamellae, indicating that this is a stable domain texture for this material.

In addition to the presence of domain walls, we observed a number of more complex textures in the XMCD contrast, as highlighted by the blue box in Fig. 5(b) and indicated by arrows in (d). In particular, isolated configurations with a three-fold symmetry cartwheel-like contrast are observed, with the XMCD changing contrast six times as one follows a line around the central points (indicated by blue arrows). Again, considering the symmetry of the XMCD contrast, such features are consistent with the presence

of topological textures that exhibit 360° winding of the Néel vector, such as the vortices and antivortices that are shown schematically in Fig. 5(d). Although XMCD measurements alone are insufficient to distinguish between vortices and antivortices of opposite winding, the observed contrast indicates the presence of such topological magnetic textures in bulk altermagnets. The presence of such winding textures has been observed in hexagonal compensated magnets in thin films—both MnTe [35], and hematite [61]. Their observation here highlights that such textures can also spontaneously occur in lamellae extracted from single crystals, indicating that they are at least a metastable configuration.

VI. CONCLUSION

In conclusion, we have obtained experimental evidence for altermagnetic order in bulk MnTe. By performing nanoscale XMCD imaging in transmission on a 150–200 nm-thick lamella extracted from a bulk crystal, we observe altermagnetic domains, domain walls and winding topological textures with a spectroscopic signature characteristic of altermagnetic order in bulk MnTe. Comparison of the XMCD signal with the LDA+DMFT AIM calculations [34] reveals excellent quantitative agreement, indicating that this altermagnetic order exists through the thickness of the lamella and is not confined to the surface, confirming the bulk nature of the state.

This experimental evidence of altermagnetic ordering in the bulk provides an important insight for future studies of altermagnetic phenomena. The consistency of the XMCD spectrum measured here from bulk crystals with thin films grown by MBE indicates that the order is robust to strain effects originating from the substrate in such thin films, providing evidence for the intrinsic nature of altermagnetism in MnTe. With these results, we further demonstrate that XMCD spectroscopy is a robust quantitative technique to probe altermagnetic order and, when combined with nanoscale imaging, provides a route to probing individual altermagnetic domains within complex configurations. This ability to investigate and characterize altermagnetic order in bulk crystals will constitute an important tool for the exploration and understanding of altermagnetism across a wide range of candidate materials, of key importance for the development of future technologies.

Finally, the measurement of XMCD in transmission allows for the probing of bulk order through the thickness of a sample. Going forward, this could be combined with vector dichroic tomographic methods [60,62] combining linear and circular dichroism to map three-dimensional altermagnetic configurations. We note that here, a lamella of 200 nm thickness was measured, which is associated with 20% transmission on resonance, thus limiting the on resonance imaging to thin systems. However, due to the oscillating nature of the XMCD signal, considerable XMCD is also found in the pre-edge as seen in Fig. 4(c), where there is significantly higher transmission, offering a route to visualizing altermagnetic configurations in micrometer-thick systems [63]. Lastly, we note that one of the advantages of transmission x-ray imaging is that due to its photon-in, photon-out nature, it can be easily combined with *in situ* measurements. The combination with transport measurements, electrical stimuli, and the application of magnetic fields should provide a route to determining the microscopic origin of the anomalous Hall effect measured in altermagnets, as well as exploring the manipulation of altermagnetic textures on the nanoscale.

ACKNOWLEDGMENTS

We thank the Helmholtz Zentrum Berlin für Materialien und Energie and the ESRF (ID 22 beamline) for the allocation of synchrotron radiation beamtime. R.Y., L.T., M.D.P.M., J.C.C.F. and C.D. acknowledge funding from the Max Planck Society Lise Meitner Excellence Program and funding from the European Research Council (ERC) under ERC Starting Grant No. 3DNANOQUANT 101116043. L.T. and M.D.P.M. acknowledge the support of the Alexander von Humboldt Foundation. S.F. acknowledges funding from the Swiss National Science Foundation under Grant No. IZSEZ0_223146. The authors thank Seunghyun Khim for support with Laue measurements and Vicky Hasse for support with the synthesis of the samples.

DATA AVAILABILITY

The data that support the findings of this article are openly available [64].

APPENDIX A: GROWTH OF MANGANESE TELLURIDE SINGLE CRYSTALS AND X-RAY CHARACTERIZATION

First, MnTe was synthesized by a direct reaction of Mn (pieces, Chempur 99.99%, powdered directly before use) and Te (powder, Alfa Aesar 99.999%) in an equimolar ratio, with the addition of 1.5 mg/ml ampoule volume of iodine (Alfa Aesar 99.998%) at 500°C in evacuated quartz glass tubes for 10 days. Following this, MnTe crystals were grown from the resulting microcrystalline powder by chemical vapor transport in a temperature gradient from 700°C (source) to 650°C (sink) with iodine (Alfa Aesar 99.998%) 1.5 mg/ml as a transport agent.

The crystal structure of the MnTe was identified by single crystal and powder x-ray diffraction. For the first investigation, a sample with an irregular shape and dimensions of approximately 0.05 mm was mechanically extracted from a grown crystal. For characterization using the powder method, several crystals were pulverized and the resulting powder was placed in a glass capillary with a diameter

of 0.3 mm. Data were collected at the ID22 beamline of the European Synchrotron Radiation Facility. The hexagonal structure of NiAs type was confirmed with the following parameters: space group $P6_3/mmc$ (No. 194), $a = 4.1483(1)$ Å, $c = 6.7162(3)$ Å, Mn at $2a$ $(0, 0, 0)$, Te at $2c$ $(\frac{1}{3}, \frac{2}{3}, \frac{1}{4})$. The refinement of the occupation of both positions (Mn and Te) did not indicate any deviation from the stoichiometric 1 : 1 composition. The crystal structure images were produced using the VESTA program [65].

APPENDIX B: PREPARATION OF LAMELLA WITH FOCUSED ION BEAM

The MnTe lamella was extracted from a bulk single crystal using a focused Ga ion beam. A standard liftout method, utilizing an *in situ* micromanipulator, was employed, and the sample was mounted onto a copper transmission electron microscopy grid, where it was further thinned to 150–200 nm. The lamella was oriented with the c axis normal to the plane. The orientation of the lamella with respect to the crystallographic orientation was determined by performing Laue measurements on the crystal from which the lamella was extracted.

APPENDIX C: SCANNING TRANSMISSION X-RAY MICROSCOPY

Scanning transmission x-ray microscopy was carried out at the MAXYMUS endstation at the BESSY-II synchrotron operated by Helmholtz-Zentrum Berlin für Materialien und Energie. Using a Fresnel zone plate and order-selecting aperture, the x-ray beam was focused to a spot size of approximately 25 nm. The sample was cooled in the absence of external magnetic fields to 100 K using an *in-situ* helium cryostat. To acquire images, the sample was scanned through the x-ray beam using a piezoelectric motor stage, with the transmission measured pixel by pixel using an avalanche photodiode. Sequential images of both positive and negative x-ray circular polarization were acquired as a function of energy across the Mn $L_{2,3}$ edges, in order to track and exploit the XMCD.

APPENDIX D: CALCULATION OF XMCD

The x-ray magnetic circular dichroism images presented in this paper were calculated in the following way. The transmitted intensity of circularly polarized x-rays ($I^{\pm}$), measured in the experiment, is given by

$$I^{\pm} = I_0 e^{-\mu^{\pm} d}, \tag{D1}$$

where I_0 is the incident intensity, $\mu^{\pm}$ is the energy- and magnetism-dependent attenuation coefficient for positive (negative) circular polarized x-rays, and d is the thickness of the sample. The normalized intensity is defined as

$$I^{\pm}_{\text{norm}} = I^{\pm}/I_0, \tag{D2}$$

The XMCD signal is calculated as

$$\text{XMCD} = 100 \times \frac{I^{+}_{\text{norm}} - I^{-}_{\text{norm}}}{A_{\text{max}}}\%. \tag{D3}$$

Here, A_{max} is the maximum absorption of the material at the L_3 edge (see Fig. 4). Calculating the XMCD as a percentage of this value allows us to obtain thickness-independent values for the XMCD. These values can then be quantitatively compared with different energies, and furthermore can be compared with predicted XMCD values from the LDA+DMFT AIM calculations [34].

[1] L. Bai, W. Feng, S. Liu, L. Šmejkal, Y. Mokrousov, and Y. Yao, Altermagnetism: Exploring new frontiers in magnetism and spintronics, Adv. Funct. Mater. **34**, 2409327 (2024).

[2] K.-W. Kim, B.-G. Park, and K.-J. Lee, Spin current and spin-orbit torque induced by ferromagnets, npj Spintronics **2**, 8 (2024).

[3] F. Giustino *et al.*, The 2021 quantum materials roadmap, J. Phys.: Mater. **3**, 042006 (2021).

[4] R. Cheng, D. Xiao, and A. Brataas, Terahertz antiferromagnetic spin Hall nano-oscillator, Phys. Rev. Lett. **116**, 207603 (2016).

[5] H. Qiu, T. S. Seifert, L. Huang, Y. Zhou, Z. Kašpar, C. Zhang, J. Wu, K. Fan, Q. Zhang, D. Wu, T. Kampfrath, C. Song, B. Jin, J. Chen, and P. Wu, Terahertz spin current dynamics in antiferromagnetic hematite, Adv. Sci. **10**, 2300512 (2023).

[6] T. Jungwirth, X. Marti, P. Wadley, and J. Wunderlich, Antiferromagnetic spintronics, Nat. Nanotechnol. **11**, 231 (2016).

[7] L. Šmejkal, J. Sinova, and T. Jungwirth, Beyond conventional ferromagnetism and antiferromagnetism: A phase with nonrelativistic spin and crystal rotation symmetry, Phys. Rev. X **12**, 031042 (2022).

[8] L. Šmejkal, J. Sinova, and T. Jungwirth, Emerging research landscape of altermagnetism, Phys. Rev. X **12**, 040501 (2022).

[9] I. Gray, Q. Deng, Q. Tian, M. Chilcote, J. S. Dodge, M. Brahlek, and L. Wu, Time-resolved magneto-optical effects in the altermagnet candidate MnTe, Appl. Phys. Lett. **125**, 212404 (2024).

[10] A. Dal Din, O. J. Amin, P. Wadley, and K. W. Edmonds, Antiferromagnetic spintronics and beyond, npj Spintronics **2**, 1 (2024).

[11] L. Šmejkal, R. González-Hernández, T. Jungwirth, and J. Sinova, Crystal time-reversal symmetry breaking and spontaneous Hall effect in collinear antiferromagnets, Sci. Adv. **6**, eaaz8809 (2020).

[12] K. Samanta, M. Ležaić, M. Merte, F. Freimuth, S. Blügel, and Y. Mokrousov, Crystal Hall and crystal magneto-optical effect in thin films of $SrRuO_3$, J. Appl. Phys. **127**, 213904 (2020).

[13] M. Naka, S. Hayami, H. Kusunose, Y. Yanagi, Y. Motome, and H. Seo, Anomalous Hall effect in κ-type organic antiferromagnets, Phys. Rev. B **102**, 075112 (2020).

[14] Z. Feng, X. Zhou, L. Šmejkal, L. Wu, Z. Zhu, H. Guo, R. González-Hernández, X. Wang, H. Yan, P. Qin, X. Zhang, H. Wu, H. Chen, Z. Meng, L. Liu, Z. Xia, J. Sinova, T. Jungwirth, and Z. Liu, An anomalous Hall effect in altermagnetic ruthenium dioxide, Nat. Electron. **5**, 735 (2022).

[15] M. Naka, S. Hayami, H. Kusunose, Y. Yanagi, Y. Motome, and H. Seo, Spin current generation in organic antiferromagnets, Nat. Commun. **10**, 4305 (2019).

[16] R. González-Hernández, L. Šmejkal, K. Výborný, Y. Yahagi, J. Sinova, T. Jungwirth, and J. Železný, Efficient electrical spin splitter based on nonrelativistic collinear antiferromagnetism, Phys. Rev. Lett. **126**, 127701 (2021).

[17] Y. Noda, K. Ohno, and S. Nakamura, Momentum-dependent band spin splitting in semiconducting MnO_2: A density functional calculation, Phys. Chem. Chem. Phys. **18**, 13294 (2016).

[18] T. Okugawa, K. Ohno, Y. Noda, and S. Nakamura, Weakly spin-dependent band structures of antiferromagnetic perovskite $LaMO_3$ (M = Cr, Mn, Fe), J. Phys.: Condens. Matter **30**, 075502 (2018).

[19] K.-H. Ahn, A. Hariki, K.-W. Lee, and J. Kuneš, Antiferromagnetism in RuO_2 as d-wave Pomeranchuk instability, Phys. Rev. B **99**, 184432 (2019).

[20] S. Hayami, Y. Yanagi, and H. Kusunose, Momentum-dependent spin splitting by collinear antiferromagnetic ordering, J. Phys. Soc. Jpn. **88**, 123702 (2019).

[21] L.-D. Yuan, Z. Wang, J.-W. Luo, E. I. Rashba, and A. Zunger, Giant momentum-dependent spin splitting in centrosymmetric low-z antiferromagnets, Phys. Rev. B **102**, 014422 (2020).

[22] S. Hayami, Y. Yanagi, and H. Kusunose, Bottom-up design of spin-split and reshaped electronic band structures in antiferromagnets without spin-orbit coupling: Procedure on the basis of augmented multipoles, Phys. Rev. B **102**, 144441 (2020).

[23] L.-D. Yuan, Z. Wang, J.-W. Luo, and A. Zunger, Prediction of low-z collinear and noncollinear antiferromagnetic compounds having momentum-dependent spin splitting even without spin-orbit coupling, Phys. Rev. Mater. **5**, 014409 (2021).

[24] H. Chen, Q. Niu, and A. MacDonald, Anomalous Hall effect arising from noncollinear antiferromagnetism, Phys. Rev. Lett. **112**, 017205 (2014).

[25] J. Kübler and C. Felser, Non-collinear antiferromagnets and the anomalous Hall effect, Europhys. Lett. **108**, 67001 (2014).

[26] S. Nakatsuji, N. Kiyohara, and T. Higo, Large anomalous Hall effect in a non-collinear antiferromagnet at room temperature, Nature **527**, 212 (2015).

[27] N. Sasabe, M. Kimata, and T. Nakamura, Presence of X-ray magnetic circular dichroism signal for zero-magnetization antiferromagnetic state, Phys. Rev. Lett. **126**, 157402 (2021).

[28] G. Van Der Laan, Determination of spin chirality using x-ray magnetic circular dichroism, Phys. Rev. B **104**, 094414 (2021).

[29] R. D. Gonzalez Betancourt, J. Zubáč, R. Gonzalez-Hernandez, K. Geishendorf, Z. Šobáň, G. Springholz, K. Olejník, L. Šmejkal, J. Sinova, T. Jungwirth, S. T. B. Goennenwein, A. Thomas, H. Reichlová, J. Železný, and D. Kriegner, Spontaneous anomalous Hall effect arising from an unconventional compensated magnetic phase in a semiconductor, Phys. Rev. Lett. **130**, 036702 (2023).

[30] H. Reichlova *et al.*, Observation of a spontaneous anomalous Hall response in the Mn_5Si_3 d-wave altermagnet candidate, Nat. Commun. **15**, 4961 (2024).

[31] K. P. Kluczyk, K. Gas, M. J. Grzybowski, P. Skupiński, M. A. Borysiewicz, T. Fąs, J. Suffczyński, J. Z. Domagala, K. Grasza, A. Mycielski, M. Baj, K. H. Ahn, K. Výborný, M. Sawicki, and M. Gryglas-Borysiewicz, Coexistence of anomalous Hall effect and weak magnetization in a nominally collinear antiferromagnet MnTe, Phys. Rev. B **110**, 155201 (2024).

[32] L. Šmejkal, A. H. MacDonald, J. Sinova, S. Nakatsuji, and T. Jungwirth, Anomalous Hall antiferromagnets, Nat. Rev. Mater. **7**, 482 (2022).

[33] J. Krempaský *et al.*, Altermagnetic lifting of Kramers spin degeneracy, Nature **626**, 517 (2024).

[34] A. Hariki, A. Dal Din, O. J. Amin, T. Yamaguchi, A. Badura, D. Kriegner, K. W. Edmonds, R. P. Campion, P. Wadley, D. Backes, L. S. I. Veiga, S. S. Dhesi, G. Springholz, L. Šmejkal, K. Výborný, T. Jungwirth, and J. Kuneš, X-ray magnetic circular dichroism in altermagnetic α-MnTe, Phys. Rev. Lett. **132**, 176701 (2024).

[35] O. J. Amin *et al.*, Nanoscale imaging and control of altermagnetism in MnTe, Nature **636**, 348 (2024).

[36] L. Smejkal, R. Gonzalez-Hernandez, T. Jungwirth, and J. Sinova, Crystal time-reversal symmetry breaking and spontaneous Hall effect in collinear antiferromagnets, Sci. Adv. **6**, eaaz8809 (2020).

[37] T. Berlijn, P. C. Snijders, O. Delaire, H.-D. Zhou, T. A. Maier, H.-B. Cao, S.-X. Chi, M. Matsuda, Y. Wang, M. R. Koehler, P. R. C. Kent, and H. H. Weitering, Itinerant antiferromagnetism in RuO_2, Phys. Rev. Lett. **118**, 077201 (2017).

[38] Z. H. Zhu, J. Strempfer, R. R. Rao, C. A. Occhialini, J. Pelliciari, Y. Choi, T. Kawaguchi, H. You, J. F. Mitchell, Y. Shao-Horn, and R. Comin, Anomalous antiferromagnetism in metallic RuO_2 determined by resonant x-ray scattering, Phys. Rev. Lett. **122**, 017202 (2019).

[39] O. Fedchenko *et al.*, Observation of time-reversal symmetry breaking in the band structure of altermagnetic RuO_2, Sci. Adv. **10**, eadj4883 (2024).

[40] Z. Lin, D. Chen, W. Lu, X. Liang, S. Feng, K. Yamagami, J. Osiecki, M. Leandersson, B. Thiagarajan, J. Liu, C. Felser, and J. Ma, Observation of giant spin splitting and d-wave spin texture in room temperature altermagnet RuO_2, arXiv:2402.04995 [cond-mat.mtrl-sci].

[41] M. Hiraishi, H. Okabe, A. Koda, R. Kadono, T. Muroi, D. Hirai, and Z. Hiroi, Nonmagnetic ground state in RuO_2 revealed by muon spin rotation, Phys. Rev. Lett. **132**, 166702 (2024).

[42] P. Keßler, L. Garcia-Gassull, A. Suter, T. Prokscha, Z. Salman, D. Khalyavin, P. Manuel, F. Orlandi, I. I. Mazin, R. Valentí, and S. Moser, Absence of magnetic order in RuO_2: insights from μSR spectroscopy and neutron diffraction, npj Spintronics **2**, 50 (2024).

[43] J. Liu *et al.*, Absence of altermagnetic spin splitting character in rutile oxide RuO_2, Phys. Rev. Lett. **133**, 176401 (2024).

[44] N. Kunitomi, Y. Hamaguchi, and S. Anzai, Neutron diffraction study on manganese telluride, J. Phys. **25**, 568 (1964).

[45] S. Lee, S. Lee, S. Jung, J. Jung, D. Kim, Y. Lee, B. Seok, J. Kim, B. G. Park, L. Šmejkal, C.-J. Kang, and C. Kim, Broken kramers degeneracy in altermagnetic MnTe, Phys. Rev. Lett. **132**, 036702 (2024).

[46] D. Takegami, T. Aoyama, T. Okauchi, T. Yamaguchi, S. Tippireddy, S. Agrestini, M. García-Fernández, T. Mizokawa, K. Ohgushi, K.-J. Zhou, J. Chaloupka, J. Kuneš, A. Hariki, and H. Suzuki, Circular dichroism in resonant inelastic x-ray scattering: Probing altermagnetic domains in MnTe, arXiv:2502.10809 [cond-mat.str-el].

[47] S. Bey, S. S. Fields, N. G. Combs, B. G. Márkus, D. Beke, J. Wang, A. V. Ievlev, M. Zhukovskyi, T. Orlova, L. Forró, S. P. Bennett, X. Liu, and B. A. Assaf, Unexpected tuning of the anomalous Hall effect in altermagnetic MnTe thin films, arXiv:2409.04567 [cond-mat.mtrl-sci].

[48] A. Chakraborty, R. González Hernández, L. Šmejkal, and J. Sinova, Strain-induced phase transition from antiferromagnet to altermagnet, Phys. Rev. B **109**, 144421 (2024).

[49] C. Chen, X. He, Q. Xiong, C. Quan, H. Hou, S. Ji, J. Yang, and X. Li, Strain-modulated valley polarization and piezomagnetic effects in altermagnetic Cr_2S_2, arXiv:2410.17686 [cond-mat.mtrl-sci].

[50] T. Osumi, S. Souma, T. Aoyama, K. Yamauchi, A. Honma, K. Nakayama, T. Takahashi, K. Ohgushi, and T. Sato, Observation of a giant band splitting in altermagnetic MnTe, Phys. Rev. B **109**, 115102 (2024).

[51] O. de Melo, F. Leccabue, C. Pelosi, V. Sagredo, M. Chourio, J. Martin, G. Bocelli, and G. Calestani, Crystal growth and characterization of MnTe single crystals, J. Cryst. Growth **110**, 445 (1991).

[52] A. N. Bogdanov and I. E. Dragunov, Metastable states, spin–reorientation transitions, and domain structures in planar hexagonal antiferromagnets, Low Temp. Phys. **24**, 852 (1998).

[53] D. Kriegner, K. Výborný, K. Olejník, H. Reichlová, V. Novák, X. Marti, J. Gazquez, V. Saidl, P. Němec, V. V. Volobuev, G. Springholz, V. Holý, and T. Jungwirth, Multiple-stable anisotropic magnetoresistance memory in antiferromagnetic MnTe, Nat. Commun. **7**, 11623 (2016).

[54] A. Hariki, T. Uozumi, and J. Kuneš, LDA+DMFT approach to core-level spectroscopy: Application to 3d transition metal compounds, Phys. Rev. B **96**, 045111 (2017).

[55] A. Hariki, M. Winder, and J. Kuneš, Continuum charge excitations in high-valence transition-metal oxides revealed by resonant inelastic x-ray scattering, Phys. Rev. Lett. **121**, 126403 (2018).

[56] A. Hariki, M. Winder, T. Uozumi, and J. Kuneš, LDA + DMFT approach to resonant inelastic x-ray scattering in correlated materials, Phys. Rev. B **101**, 115130 (2020).

[57] E. Folven, A. Scholl, A. Young, S. T. Retterer, J. E. Boschker, T. Tybell, Y. Takamura, and J. K. Grepstad, Effects of nanostructuring and substrate symmetry on antiferromagnetic domain structure in $LaFeO_3$ thin films, Phys. Rev. B **84**, 220410 (2011).

[58] S. Reimers *et al.*, Magnetic domain engineering in antiferromagnetic CuMnAs and Mn_2Au, Phys. Rev. Appl. **21**, 064030 (2024).

[59] H. Gomonay and V. M. Loktev, Magnetostriction and magnetoelastic domains in antiferromagnets, J. Phys.: Condens. Matter **14**, 3959 (2002).

[60] C. Donnelly, M. Guizar-Sicairos, V. Scagnoli, S. Gliga, M. Holler, J. Raabe, and L. J. Heyderman, Three-dimensional magnetization structures revealed with x-ray vector nanotomography, Nature **547**, 328 (2017).

[61] H. Jani, J. Harrison, S. Hooda, S. Prakash, P. Nandi, J. Hu, Z. Zeng, J.-C. Lin, C. Godfrey, G. ji Omar, T. A. Butcher, J. Raabe, S. Finizio, A. V.-Y. Thean, A. Ariando, and P. G. Radaelli, Spatially reconfigurable antiferromagnetic states in topologically rich free-standing nanomembranes, Nat. Mater. **23**, 619 (2024).

[62] A. Apseros, V. Scagnoli, M. Holler, M. Guizar-Sicairos, Z. Gao, C. Appel, L. J. Heyderman, C. Donnelly, and J. Ihli, X-ray linear dichroic tomography of crystallographic and topological defects, Nature **636**, 354 (2024).

[63] J. Neethirajan, B. J. Daurer, M. Di Pietro Martínez, A. Hrabec, L. Turnbull, R. Yamamoto, M. Ferreira Raboni, A. Štefančič, D. A. Mayoh, G. Balakrishnan, Z. Pei, P. Xue, L. Chang, E. Ringe, R. Harrison, S. Valencia, M. Kazemian, B. Kaulich, and C. Donnelly, Soft x-ray phase nanomicroscopy of micrometer-thick magnets, Phys. Rev. X **14**, 031028 (2024).

[64] R. Yamamoto *et al.*, Altermagnetic nanotextures revealed in bulk MnTe, Zenodo (2025), https://doi.org/10.5281/zenodo.16803814.

[65] K. Momma and F. Izumi, *VESTA3* for three-dimensional visualization of crystal, volumetric and morphology data, J. Appl. Cryst. **44**, 1272 (2011).